ACS APPLIED MATERIALS & INTERFACES

RESEARCH ARTICLE

www.acsami.org

Scanning Thermal Lithography of Tailored *tert*-Butyl Ester Protected Carboxylic Acid Functionalized (Meth)acrylate Polymer Platforms

Joost Duvigneau, Holger Schönherr,*,† and G. Julius Vancso*

MESA+ Institute for Nanotechnology and Faculty of Science and Technology, Department of Materials Science and Technology of Polymers, University of Twente, P.O. Box 217, 7500 AE Enschede, The Netherlands

Supporting Information

ABSTRACT: In this paper, we report on the development of tailored polymer films for high-resolution atomic force microscopy based scanning thermal lithography (SThL). In particular, full control of surface chemical and topographical structuring was sought. Thin cross-linked films comprising poly(*tert*-butyl methacrylate) (MA_{20}) or poly(*tert*-butyl acrylate) (A_{20}) were prepared via UV initiated free radical polymerization. Thermogravimetric analysis (TGA) and FTIR spectroscopy showed that the heat-induced thermal decomposition of MA_{20} by oxidative depolymerization is initially the primary reaction followed by *tert*-butyl ester thermolysis. By contrast, no significant depolymerization was observed for A_{20}. For A_{20} and MA_{20} (at higher temperatures and/or longer reaction times) the thermolysis of the *tert*-butyl ester liberates isobutylene and yields carboxylic acid groups, which react further intramolecularly to cyclic anhydrides. The values of the apparent activation energies (E_a) for the thermolysis were calculated to be 125 ± 13 kJ mol^{-1} and 116 ± 7 kJ mol^{-1} for MA_{20} and A_{20}, respectively. Both MA_{20} and A_{20} films showed improved thermomechanical stability during SThL compared to non cross-linked films. Carboxylic acid functionalized lines written by SThL in A_{20} films had a typically ~10 times smaller width compared to those written in MA_{20} films regardless of the tip radius of the heated probe and did not show any evidence for thermochemically or thermomechanically induced modification of film topography. These observations and the E_a of 45 ± 3 kJ mol^{-1} for groove formation in MA_{20} estimated from the observed volume loss are attributed to oxidative thermal depolymerization during SThL of MA_{20} films, which is considered to be the dominant reaction mechanism for MA_{20}. The smallest line width values obtained for MA_{20} and A_{20} films with SThL were 83 ± 7 nm and 21 ± 2 nm, whereas the depth of the lines was below 1 nm, respectively.

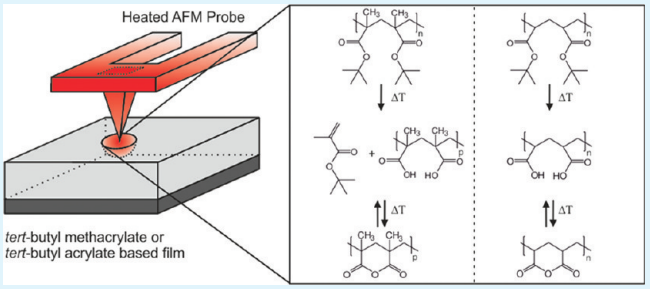

KEYWORDS: scanning thermal lithography, polymer platform, thermal chemical functionalization

1. INTRODUCTION

Scanning probe lithography (SPL) is among the most versatile tools to fabricate, manipulate and address surface domains with distinguished chemical and/or topological properties at the critical sub-100 nm length scale.[1−4] Surface-exposed domains that contain a specific type of information or functionality at these length scales are of great interest in different areas, e.g. cell-surface interaction studies,[5−8] development of (bio)sensors,[9−12] and data storage applications.[13,14] Compared to other direct writing nanofabrication techniques (i.e., directed beam lithographies),[15,16] SPL is relatively cost-effective and easy to operate in a broad range of environments on a wide variety of samples, including organic and biological materials. The serial nature of SPL has been addressed by the development of cantilever arrays in which thousands of cantilevers are operated in parallel.[17−19] As potential alternatives, other recently established nanolithography approaches include soft lithography[20−22] and nano imprint lithography (NIL).[23−26] The various techniques of soft lithography mainly focus on the fabrication of chemical functional surface patterns in the sub micrometer range via printing with patterned elastomer stamps. NIL utilizes specially designed topographical nano patterned molds to imprint polymer films at elevated temperatures with sub 50 nm resolution. During imprinting at elevated temperatures thermal decomposition or other thermally induced reactions may take place, which are often undesired and potentially result in distorted pattern formation.

Therefore it is not surprising that thermally induced reactions, especially surface reactions on polymers, represent a class of yet largely unexplored reactions in terms of controlled surface modification and structuring. Nealey and co-workers[27,28] induced a cylindrical to spherical morphology transition in poly(styrene)-*block*-poly(*tert*-butyl acrylate) (PS-*b*-P*t*BA) thin films by thermal cleavage of the *tert*-butyl ester. Böker et al.[29,30] reported on the thermal functionalization of poly(styrene)-*block*-poly(isoprene[*graft*-perfluoroacyl]) block

Received: May 26, 2011
Accepted: September 15, 2011
Published: September 15, 2011

copolymer surfaces via thermal cleavage of the perfluorinated side chains at 340 °C. Only Böker et al. mentioned the possible surface derivatization of exposed chemical functional groups after thermolysis. Recently we have introduced the combined thermal chemical surface functionalization and topographic patterning of PS-*b*-P*t*BA films for the development of topographically shaped chemically functional (bio)reactive interfaces. This technique is referred to as reactive imprint lithography (RIL)[31] and comprises the imprinting of PS-*b*-P*t*BA films with topographical patterned poly(dimethylsiloxane) (PDMS) stamps. The thermolysis reaction at temperatures above the thermal deprotection temperature of the *tert*-butyl ester groups renders the polymer film surfaces functionalized with carboxylic acid moieties for further derivatization with e.g. biologically relevant molecules. PS-*b*-P*t*BA block copolymer films were additionally exploited in scanning thermal lithography (SThL), which was introduced as a promising approach for the spatially controlled and highly localized thermal chemical deprotection of surface exposed *tert*-butyl esters.[32] PS-*b*-P*t*BA block copolymer films were introduced previously by our group as robust and versatile (bio)reactive platforms that could be wet chemically or thermally activated prior to aqueous derivatization with biologically relevant molecules.[33−36] Despite the robustness of the PS-*b*-P*t*BA platforms, carboxylic acid functional domains smaller than ∼400 nm × ∼600 nm were not achieved via SThL. This was ascribed to polymer deformation occurring at probe tip temperatures (T_{tip}) that are applied during writing with SThL, which exceed the polymer's glass transition temperature. Hence, the resulting morphology[32] is the result of both the thermochemical deprotection, as well as the thermomechanical deformation (i.e., rim formation). In related work, King and co-workers reported on the heated probe induced thermal chemical surface functionalization of specially designed, cross-linked copolymer films yielding surface exposed carboxylic acid[37] or amine moieties.[38] Despite photo cross-linking of the films, topographic deformations, though smaller compared to those previously observed for SThL on poly(tetra-hydropyranyl methacrylate) homopolymer films, remained (see the Supporting Information of ref 12). At the reported high tip velocities (>85 μm s^{-1}) and temperatures (>160 °C) used for SThL, formation of rims was observed exhibiting heights >10 nm.

Here we investigate the applicability of cross-linked *tert*-butyl ester containing methacrylate and acrylate based polymer films for high resolution thermal chemical surface functionalization with SThL. The fundamental differences in thermal chemical decomposition mechanisms of methacrylates and acrylates afforded full control over thermally induced surface chemical and topographical changes; in particular, exclusive surface chemical activation in the absence of topographic structuring was achieved, hence complementing the SThL approaches known to date.

2. EXPERIMENTAL METHODS

2.1. Materials. Ethylene glycol dimethacrylate (EGDMA), *tert*-butyl methacrylate (*t*BMA), *tert*-butyl acrylate (*t*BA), 1,4-dibutanol diacrylate (dBDA), 1-ethyl-3-(3-dimethylaminopropyl)carbodiimide hydrochloride (EDC), *N*-hydroxysuccinimide (NHS) and fluoresceinamine isomer I (λ_{max} = 496 nm) were bought from Sigma Aldrich (St Louis, MO, USA). Ethanol was purchased from Biosolve (Valkenswaard, The Netherlands). Amine functionalized eFluor 605NC (λ_{ex} = 350−500 nm) CdSe core quantum dots were obtained from eBioscience, Inc. (San Diego, CA, USA) and Irgacure 184 (Ciba NV, Maastricht, The Netherlands) was a generous gift from ICH Zaanstad BV (Wormerveer, The Netherlands). Phosphate buffered saline solution (PBS, pH 7.4) was bought from B. Braun (Melsungen, Germany). Milli-Q water was produced by a Millipore Synergy system (Billireca, MA, USA). PS$_n$-*b*-P*t*BA$_m$ (with degrees of polymerization *n* and *m* of 2092 and 1055, respectively) was purchased from Polymer Source Inc. (Dorval, Canada). Poly(isobutylene) (M_n ≈ 2900 g mol^{-1} and PDI ≈ 1.23) was obtained from Polymer Standards Service GmbH (Mainz, Germany). All chemicals were used as received.

2.2. Film Preparation. Glass slides were cleaned in piranha solution (1:3 (v/v) solution of 30% H_2O_2 and concentrated H_2SO_4) for 10 min and rinsed with copious amounts of Milli-Q water and ethanol followed by spin drying prior to use. ***Caution:*** *Piranha solution should be handled with extreme caution. It has been reported to detonate unexpectedly.* Silicon wafers were rinsed with ethanol and dried under a nitrogen stream, prior to use. In a typical procedure, monomer mixtures comprising 80 wt % *t*BMA and 20 wt % EGDMA (for MA$_{20}$ films) or 80 wt % *t*BA and 20 wt % dBDA (for A$_{20}$ films) were prepared in a glass vial prior to polymerization. To these mixtures 3 wt % of Irgacure 184 as photo initiator was added. Subsequently the monomer mixture was purged with nitrogen. About 0.10 mL of the monomer solution was deposited in the middle of a 26 mm × 76 mm microscopy glass slide (Menzel-Glaser, Braunschweig, Germany) or a ∼20 mm × 40 mm piece of silicon wafer (CZ, type P, boron, ⟨100⟩, thickness =525 μm, OKMETIC, Vantaa, Finland). Subsequently, the solution was covered by placing a microscopy glass slide in perpendicular orientation on top of the first slide/silicon support. The monomer mixture was allowed to spread between the two slides. Then the samples were UV irradiated by an array of 6 UV−B lamps (15 W, G15T8E, λ = 306 nm, Ushio, Tokyo, Japan, sample to lamp distance 5 cm) under a nitrogen atmosphere for 30 min to polymerize and complete film formation. Finally, the two slides were carefully separated to yield films with approximately 5 μm thickness. Bulk samples were prepared according to the same procedure in aluminum differential scanning calorimetry (DSC) pans (ALUM, Perkin-Elmer, Waltham, MA, USA), which were filled with the corresponding monomer solutions and covered by a glass microscopy slide.

2.3. Fourier Transform Infrared (FTIR) Spectroscopy. Single reflection attenuated total reflection (ATR) mode FTIR spectra (spectral resolution 4 cm^{-1}, 512 scans) were collected with a Bruker model ALPHA FTIR spectrometer equipped with an ATR platinum diamond 1 reflection crystal (Bruker Optik GmbH, Ettlingen, Germany). Background spectra were recorded against air.

2.4. Thermogravimetric Analysis. The isothermal weight loss of bulk MA$_{20}$ and A$_{20}$ polymer samples (∼ 8 mg) under nitrogen (flow rate 20 mL min^{-1}) was measured as a function of time for different temperatures with a Perkin-Elmer thermogravimetric analyzer (TGA 7, Waltham, MA). The initial temperature ramp from room temperature to the thermolysis temperature was set to 200 °C min^{-1}. The non-isothermal weight loss of bulk polymerized EGDMA and dBDA samples (∼ 8 mg) under nitrogen (flow rate 20 mL min^{-1}) was measured from 50 to 450 °C with a temperature ramp of 20 °C min^{-1}.

2.5. FITR Spectroscopy of TGA Vapor Reaction Products. The vapor phase reaction products of MA$_{20}$ and A$_{20}$ samples isothermally heated at 260 °C in a thermogravimetric analyzer (nitrogen flow rate 20 mL min^{-1}, TGA 7, Waltham, MA, USA) were fed to the inlet of an open gas cell positioned in a Vertex 70 FTIR spectrometer (Bruker Optik GmbH, Ettlingen, Germany) equipped with a MCT detector. The outlet of the gas cell was connected to a vacuum pump, maintaining a slightly reduced pressure. FTIR spectra were continuously collected (spectral resolution 4 cm^{-1}, 4 scans) for 10 min. For analysis more than 30 spectra revealing the presence of reaction product were averaged. Background spectra (32 scans) were recorded against TGA outlet vapor for an empty sample pan isothermally heated to 260 °C.

2.6. Scanning Thermal Lithography. Heatable probes (type AN-2, with 200 μm long cantilevers, Anasys Instruments, Santa Barbara, CA, USA) mounted in a Dimension D3100 atomic force microscopy equipped with a hybrid scanner and a NanoScope IVa controller (Veeco/Digital Instruments (DI), Santa Barbara, CA, USA) were used for SThL. During the experiments T_{tip} was controlled with a Nano-TA2 controller (Anasys Instruments). Prior to the experiments, T_{tip} was calibrated using the following standard polymer materials: poly (ε-caprolactone) (PCL, T_m = 55 °C), poly(ethylene) (PE, T_m = 116 °C), and poly(ethylene terephthalate) (PET, T_m = 235 °C). In the calibration of the probe temperature using this procedure, the softening of the polymer substrates is determined. Because polymers do not possess a priori a defined melting point, this procedure introduced some errors, which as we note explicitly, are not relevant for the work discussed here. Recent progress in calibration of the probe temperature has been reported by Abel et al.[55]

After SThL, contact mode AFM images were taken with the same probes. Lateral force microscopy (LFM) images of the samples were recorded with a contact load of ~20 nN, while scanning the sample at 90° with respect to the long axis of the SThL cantilever. LFM images were collected at ambient atmosphere (~ 40 - 60% relative humidity). Tapping mode AFM analysis was carried out with super sharp silicon cantilevers/tips (SSS-NCHR-10, super sharp silicon, typical tip radius of ~2 nm, Nanosensors, Wetzlar, Germany). The system operating frequency was typically 10% lower than the natural resonance frequency of the cantilever in air, the free amplitude was kept constant, while the set point amplitude was approximately 85% of the free amplitude (~1.5 V).

2.7. Wet Chemical Derivatization. Following SThL the in situ formed carboxylic acid groups were activated with EDC/NHS (200 mM and 250 mM, respectively) in PBS.[31−33] After 1 h of EDC/NHS activation, the samples were rinsed 3 times with PBS and immersed in an amino functionalized eFluor 605 quantum dot solution in PBS (concentration ~1×10^{-6} M) for 3 h, protected from direct sun light. The modified films were extensively rinsed with Milli-Q water prior to drying under a nitrogen stream and stored in the dark. Thermally activated bulk samples (Mettler FP82 hotstage temperature controlled by a Mettler FP80 central processor, Mettler-Toledo BV, Tiel, The Netherlands) were immersed in a fluoresceinamine solution in PBS (concentration ~1×10^{-4} M) for 1 h, following EDC/NHS activation (200 and 250 mM, respectively, in PBS, 1 h). The fluoresceinamine functionalized samples were immersed in 50 mL of Milli-Q water for 1 h prior to rinsing with copious amounts of Milli-Q water and drying in a nitrogen stream.

2.8. (Confocal) Fluorescence Microscopy. Fluorescence microscopy images of dried fluoresceinamine modified bulk polymer samples were taken immediately after preparation of the samples with an Olypus IX71 fluorescence microscope. For the excitation of fluoresceinamine an U-MWB-2 filter cube was used, typical sample exposure times were 30 ms. Confocal fluorescence microscopy images were taken with a Carl-Zeiss LSM510 confocal laser scanning microscope (Carl Zeiss MicroImaging GmbH, Göttingen, Germany) equipped with a LP 560 filter. For the excitation of eFluor 605 quantum dots an argon-ion laser with a wavelength of 488 nm was used.

3. RESULTS AND DISCUSSION

3.1. Film Preparation. To improve the thermomechanical stability of polymer films for SThL, the development of cross-linked films based on *tert*-butyl ester protected carboxylic acid bearing monomers and difunctional (meth)acrylate cross-linkers was proposed (see the Supporting Information). The two systems developed are based on the free radical photo initiated polymerization of either *tert*-butyl methacrylate (*t*BMA) and ethylene glycol dimethacrylate (EGDMA) or *tert*-butyl acrylate (*t*BA) and 1,4 butanediol diacrylate (dBDA) monomer mixtures between two glass cover slides in the presence of a photo initiator. The prepared films are referred to as MA_x and A_x, in which MA and A denotes methacrylate and acrylate based films, respectively. The number in subscript (x) represents the wt% of cross-linker in the monomer mixture (typically, x was ~20 wt %, which corresponds to ~15 mol % for both systems).

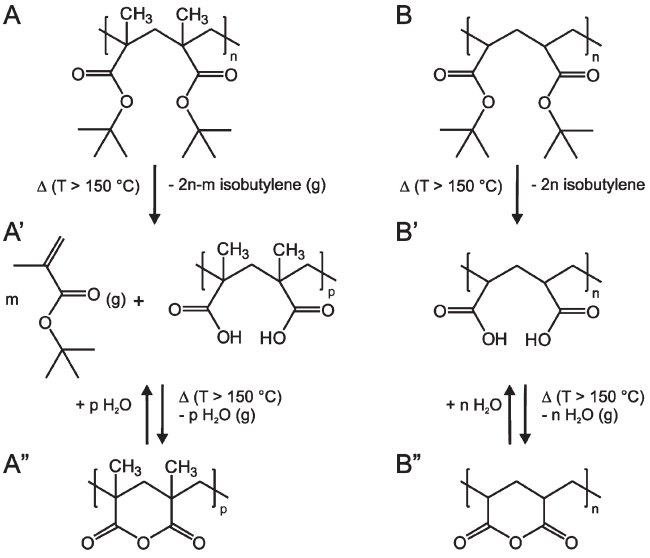

Figure 1. Thermal deprotection mechanism of MA_{20} (A) and A_{20} (B) polymer films. The decomposition of MA_{20} is initially dominated by depolymerization yielding *tert*-butyl methacrylate. Anhydride formation (A″) following ester decomposition yielding isobutylene and carboxylic acid moieties (A′) inhibits the depolymerization in a later stage of the thermal decomposition reaction. Thermolysis of A_{20} initially yields carboxylic acid groups upon the loss of isobutylene (B′) followed by the loss of water to form intramolecular anhydride groups (B″). Note: The intramolecular cyclization step (i.e., anhydride formation in A″ and B″) is limited in yield to 87% because of statistical reasons.[41,42]

3.2. Thermal Decomposition Reactions in MA_{20} and A_{20}. Despite the close resemblance of methacrylate and acrylate monomer structures their thermal degradation behavior is quite different. Methacrylates are known to show a higher degree of depolymerization at elevated temperatures compared to acrylates with the same ester substituent.[39] In Figure 1, the proposed reaction mechanisms for MA_{20} and A_{20} thermal decomposition are shown.

Grassie[39] discussed the primary thermal degradation mechanism observed in methacrylates depending on the number of β hydrogen atoms on the ester substituent. The two competing reaction mechanisms are (i) depolymerization and (ii) de-esterification with a strong autocatalytic nature[39] followed by the loss of water yielding intramolecular anhydride bonds. In general, the higher the number of β hydrogen atoms on the ester substituent, the higher is the contribution of de-esterification as the (primary) reaction mechanism upon thermal decomposition. *Tert*-butyl esters, having 9 β hydrogen atoms, are thus mainly subjected to ester decomposition with very little depolymerization upon thermal decomposition. In another paper Grant and Grassie[40] reported on the thermal decomposition of poly(*tert*-butyl methacrylate) P*t*BMA at temperatures between 180 and 200 °C. In the initial stage of the thermal decomposition reaction depolymerization yielding *tert*-butyl methacrylate monomer was found to be the primary reaction. Upon thermal decomposition of *tert*-butyl ester groups and the subsequent formation of

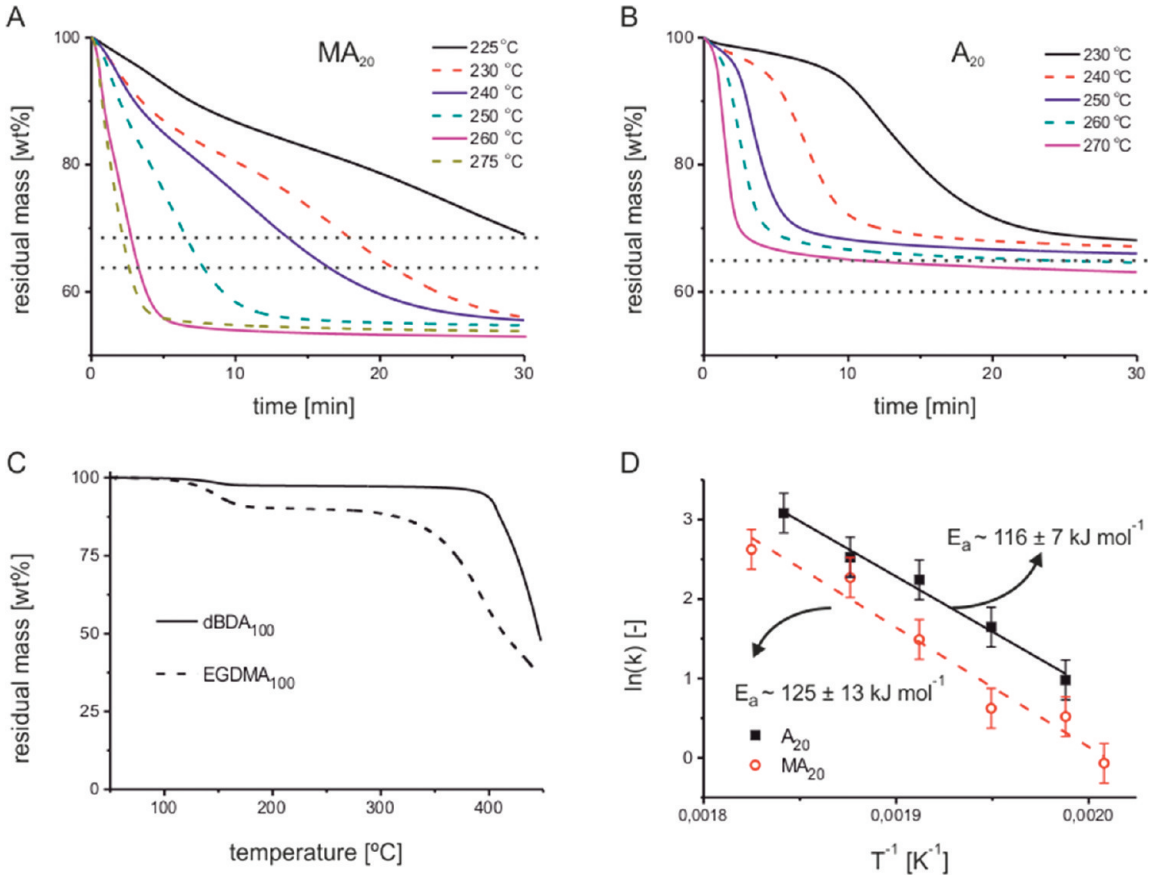

Figure 2. Isothermal TGA data of bulk samples of (A) MA_{20} and (B) A_{20} for temperatures above the thermal deprotection temperature of the ester. Heating from room temperature to the isothermal holding temperatures was applied at a rate of 200 °C min^{-1}. The horizontal dashed lines represent the theoretical expected weight loss of isobutylene (upper) and subsequently water (lower) upon thermolysis based on the actual polymer compositions. The statistically limited yield of the intramolecular cyclization is taken into account. (C) Non-isothermal TGA data of bulk polymerized EGDMA ($EGDMA_{100}$) and dBDA ($dBDA_{100}$) (at a heating rate of 20 °C min^{-1}). (D) Arrhenius plot of zero order reaction rate constants obtained from linear least-squares fits to the data shown in A and B between a residual mass of 80 to 70 wt % and 90 to 80 wt %, respectively.

intramolecular anhydride groups, polymer decomposition was inhibited. In contrast to polymethacrylates, polyacrylates typically do not undergo depolymerization reactions. It was further reported by Grant and Grassie[40] that besides the formation of isobutylene and water, no monomer traces were observed upon thermolysis of P*t*BA. De-esterification followed by the formation of intramolecular anhydride groups are hence the primary thermal decomposition mechanisms observed in P*t*BA.

In Figure 2, isothermal thermogravimetric analysis (TGA) data of MA_{20} (A) and A_{20} (B) are shown. The dashed horizontal lines in panels A and B in Figure 2 represent the theoretical residual mass for quantitative loss of isobutylene (upper) and the loss of water (lower). Obviously, the decomposition of MA_{20} for 30 min at temperatures above 230 °C results in a higher mass loss compared to the stoichiometric loss of isobutylene and water. This is in line with the occurrence of a depolymerization reaction during the initial stage of the reaction as discussed above. The presence of *tert*-butyl methacrylate monomer in the gaseous reaction products after thermal decomposition at 260 °C was confirmed with transmission FTIR spectroscopy (see the Supporting Information). The decomposition of A_{20} exhibits essentially quantitative mass loss values in accordance to the loss of isobutylene and water, which is in agreement with the mechanism presented in Figure 1. The observed slightly higher residual mass after 30 min is presumably the result of inhibition of the autocatalytic thermal ester decomposition[40] as a result of the cross-linked morphology.

In Figure 2C, TGA data of EGDMA and dBDA bulk polymer samples are shown. The acrylate cross-linker is thermally stable up to approximately 400 °C. By contrast, the methacrylate cross-linker shows a significant mass loss around 150 °C, which is in agreement with the occurrence of depolymerization reactions. The presence of cross-links in the polymer possibly prevents the completion of polymer decomposition and stabilizes the polymer sample up to temperatures of approximately 320 °C after which further thermal decomposition occurs.

To obtain the apparent ester thermolysis activation energy, we analyzed the isothermal TGA data between 70−80 and 80−90% residual mass for MA_{20} and A_{20}, respectively. The raw data suggest an overall zeroth order reaction kinetics. Linear least-squares fits to the data within the mentioned residual mass ranges confirmed the zeroth order reaction kinetics for both systems under investigation. In the analysis, the following assumptions were made: (i) Depolymerization occurs solely during the initial stage of MA_{20} decomposition. (ii) The used cross-linkers do not interfere with the thermal ester decomposition reactions. (iii) In the stated residual mass loss ranges, carboxylic acid groups and isobutylene are the primary reaction products.

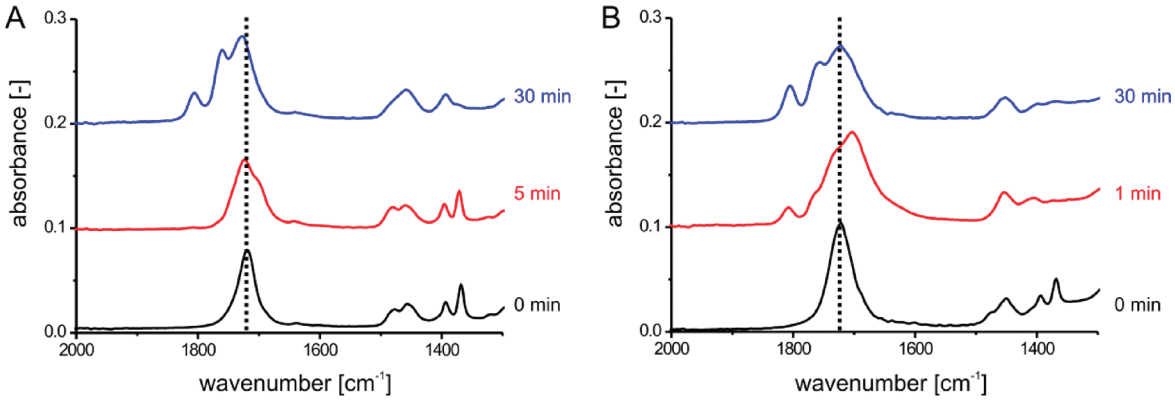

Figure 3. Single reflection ATR-FTIR spectra of MA_{20} (A) and A_{20} (B) before and after thermal decomposition at 250 °C for times up to 30 min. Upon thermolysis, the $\nu_{C=O}$ (ester at 1726 cm^{-1}) absorbance shifts to 1709 cm^{-1} ($\nu_{C=O}$ carboxylic acid) followed by a shift to 1752 cm^{-1} and 1804 cm^{-1} corresponding to $\nu_{C=O}$ (anhydride) absorbances. During thermolysis, the absorbances corresponding to δ_{C-H} (*tert*-butyl methyl) between 1350 and 1400 cm^{-1} disappear. Anhydride formation occurs at lower thermolysis times for the acrylate-based system compared to the methacrylate-based system.

Figure 2D shows a plot of the values of the zeroth order reaction rate constants k versus T^{-1} according to the Arrhenius equation

$$k = Ae^{-E_a/RT} \quad (1)$$

In which A is the pre-exponential factor, R is the gas constant (8.314 J K^{-1} mol^{-1}), and T denotes the temperature (K). The apparent activation energies (E_a) for MA_{20} and A_{20} were calculated to be 125 ± 13 and 116 ± 7 kJ mol^{-1}, respectively. These numbers are in good agreement with results reported by others for the activation energy of *tert*-butyl ester decomposition of P*t*BA.[32,43,44]

Figure 3 shows single reflection ATR-FTIR spectra of MA_{20} (A) and A_{20} (B) bulk polymer samples before and after thermolysis at 250 °C for different times, respectively. Before thermal decomposition the $\nu_{C=O}$ (ester) absorbance at 1726 cm^{-1} is clearly visible (dashed vertical lines). Upon thermolysis, the ester stretching absorbance shifts to 1709 cm^{-1}, which corresponds to $\nu_{C=O}$ (carboxylic acid) absorbances, followed by a shift to 1752 and 1804 cm^{-1} corresponding to $\nu_{C=O}$ (anhydride) absorbances. In agreement with the disappearance of the ester stretching absorbance, the δ_{C-H} (*tert*-butyl methyl) absorbance between 1350 and 1400 cm^{-1} disappears, accordingly. The observed shifts in $\nu_{C=O}$ and disappearance of δ_{C-H} (*tert*-butyl methyl) are in agreement with earlier reported results for the thermolysis of PS-*b*-P*t*BA polymer thin films.[31,32] The residual $\nu_{C=O}$ (ester) absorbances observed in both the MA_{20}, as well as in the A_{20} spectra, are related to the presence of ester groups within the used cross-linkers (see Figure 1). FTIR spectroscopy of bulk polymerized EGDMA and dBDA samples before and after thermal decomposition at 250 °C for 10 min did not show thermal ester decomposition reactions of the cross-linkers.

In addition, residual $\nu_{C=O}$ (ester) absorbances for A_{20} might partially be related to residual *tert*-butyl ester group absorbances, which would explain the residual mass observed in Figure 2B, which was slightly higher compared to the theoretical quantitative yield of isobutylene and water. Furthermore it was observed that anhydride formation occurs at shorter times for A_{20} samples compared to MA_{20} samples (compare middle FITR spectra in panels A and B in Figure 5). This is in line with the competitive decomposition reactions in MA_{20} samples during the initial stage of decomposition (i.e., depolymerization vs de-esterification).

3.3. Derivatization of Thermally Deprotected MA_{20} and A_{20} Bulk Samples. Having confirmed the reaction mechanism with TGA and FTIR spectroscopy for both MA_{20} and A_{20} the chemical functionality of the in situ formed carboxylic acid and anhydride groups was investigated with fluorescence microscopy. Fluoresceinamine was covalently immobilized to thermally deprotected and subsequently wet chemically functionalized MA_{20} and A_{20} surfaces according to the well-known EDC/NHS chemistry.[31−33]

Figure 4A shows the normalized fluorescence emission intensity counts (integrated over the pixels of the fluorescence micrographs shown) of MA_{20} and A_{20} samples modified with fluoresceinamine before and after activation at 250 °C for 30 and 60 s, respectively. With increasing activation time, the normalized intensity increases for both MA_{20} as well as for A_{20} samples. Fluoresceinamine modified MA_{20} samples show a lower emission compared to modified A_{20} samples for the same activation time and temperature. This is ascribed to the difference in mechanism for MA_{20} and A_{20} as discussed earlier. The initial depolymerization reaction for MA_{20} results in a significantly lower degree of functionalization as compared to the A_{20} in which depolymerization reactions are absent. Despite the different reaction mechanisms, both samples were successfully thermally activated and subsequently modified with fluoresceinamine following EDC/NHS activation of the in situ formed carboxylic acid moieties. Thermally activated samples without chemical activation of the carboxylic acid groups did not show significant emission after immersion in a fluoresceinamine solution.

3.4. Improved Thermal Mechanical Properties for SThL. Having established the reaction mechanism for both MA_{20} and A_{20} samples, as well as the successful derivatization with fluoresceinamine following EDC/NHS activation of the formed carboxylic acid groups, the performance of MA_{20} and A_{20} films during SThL was investigated and compared to SThL on PS-*b*-P*t*BA films. Figure 5 shows contact mode AFM height images (A-C, left) of MA_{20}, A_{20} and a PS-*b*-P*t*BA polymer film after SThL of a square or set of squares at probe tip temperatures (T_{tip}) above the thermal deprotection temperature of the *tert*-butyl ester. The absence of thermomechanical surface deformations on the cross-linked polymer films is obvious (panels A and B), especially when compared with the micrometer scale deformations observed (i.e., rims) for the block copolymer film (panel C).

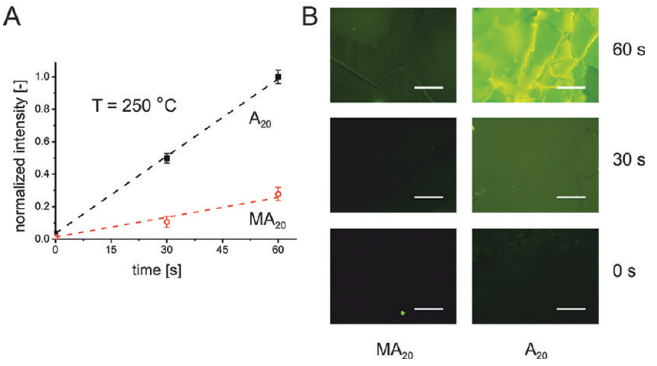

Figure 4. (A) Normalized fluorescence emission intensity as a function of thermolysis time at 250 °C for MA_{20} (open red circles) and A_{20} (filled black squares) samples covalently modified with fluoresceinamine ($\lambda_{ex} \approx 496$ nm and $\lambda_{em} \approx 520$ nm) following EDC/NHS activation. A high pressure Mercury lamp was used for excitation (λ_{ex} 460 − 490 nm). The dashed lines are a guide for the eye. In B fluorescence microscopy images of the respective samples are shown (the wrinkled appearance of the film is due to heat induced film deformation, which does not occur for SThL generated patterns). The scale bars in B represent 200 μm.

Interestingly, after SThL (T_{tip} at 260 °C, v_{tip} of 2 μm s^{-1}) on the MA_{20} surface a ∼ 15 nm deep shallow depression was observed without the formation of surrounding rims (panel A). More fascinating, after SThL on A_{20} surfaces no topographical changes were observed for 1 μm × 1 μm squares prepared with T_{tip} ranging from 260 to 280 °C and v_{tip} between 2 and 6 μm s^{-1} (panel C).

In addition to the shallow surface depression on MA_{20} films, an increase in lateral force signal was observed in the areas activated with SThL (inset in the right panel of Figure 5A), indicating the formation of a locally more hydrophilic surface area.[45−47] The observed increase in hydrophilicity is expected as a consequence of the reaction yielding carboxylic acid groups. The formation of depressions is ascribed to the loss of *t*BMA (g), resulting in localized partial decomposition of the network structure. Despite the lack of topographical changes on A_{20} films after SThL of 1 μm × 1 μm squares, the activated areas show an increase in lateral force signal (i.e., increased hydrophilicity, Figure 5B right). This is a strong indication for the localized conversion of *tert*-butyl esters to carboxylic acid groups in analogy to MA_{20} films. The observed lateral force signal as a qualitative measure of conversion shows an increase for higher T_{tip} and slower scan speeds (longer thermolysis times), as expected. The observed changes in topography and surface hydrophilicity are in full agreement with the earlier discussed decomposition mechanisms for MA_{20} and A_{20}.

Figure 6 shows a confocal fluorescence microscopy image of a 10 × 10 array of thermolyzed domains on a A_{15} film that were deprotected by tip−sample contacts in a a 10 × 10 point array with T_{tip} at 280 °C and a tip contact time of 2 s. Subsequently, the domains were covalently modified with amine functionalized eFluor 605 quantum dots (red emission) following EDC/NHS activation. Because each domain, which is topographically depressed by max. 15−20 nm (likely the result of plastic deformation in this particular SThL mode), measures approximately 420 nm by 470 nm in size, they could not be resolved individually with our fluorescence microscope. The full width half-maximum (fwhm) of the intensity profile corresponding to the overall size of the array (Figure 6B) is approximately 11 μm, which is in good

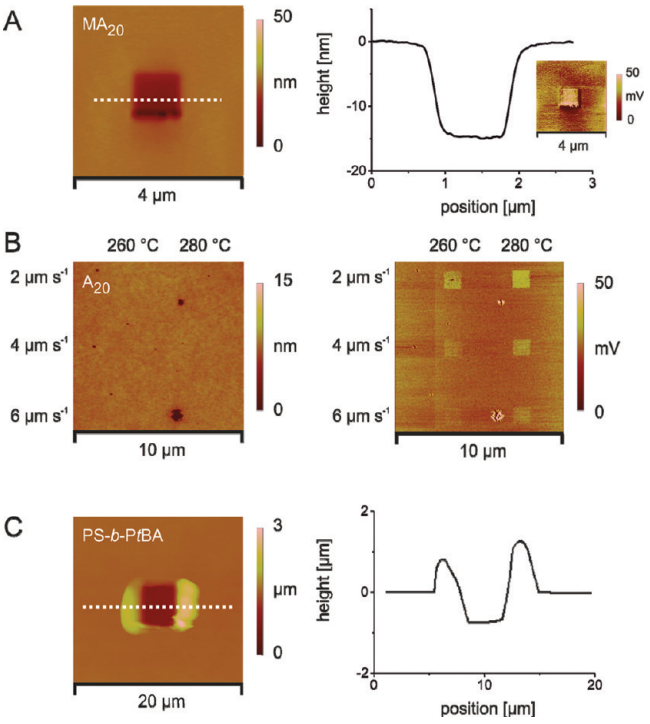

Figure 5. (A) Contact mode AFM height image (left) of MA_{20} after SThL of a 2 μm × 2 μm square with T_{tip} at 260 °C and a v_{tip} of 2 μm s^{-1}. On the right the corresponding cross-section along the white dashed line is shown. The inset shows the corresponding LFM image. (B) Contact mode AFM height (left) and lateral force (right) images of A_{20} after SThL of 1 μm × 1 μm squares with T_{tip} at 260 and 280 °C for writing speeds of 2 μm s^{-1}, 4 μm s^{-1} and 6 μm s^{-1}, respectively. (C) Contact mode AFM height image of a silicon supported PS-*b*-P*t*BA block copolymer film (left) after SThL of a 5 μm × 5 μm square with T_{tip} 265 °C and a v_{tip} of 5 μm s^{-1}. On the right the corresponding cross-section along the white dashed line is shown. The force feedback loop maintained a contact load during SThL of approximately 10, 30, and 10 nN for the results shown in A, B, and C, respectively.

agreement with the nominal overall size of the array (∼10.4 μm). The clear fluorescence signal indicates that the covalent modification with the quantum dots was very efficient.

Despite several attempts, fluorescence emission from MA_{20} films modified with fluoresceinamine was not observed in fluorescence microscopy. This is ascribed to the short deprotection times used for SThL, for which depolymerization is the primary mechanism. Hence the yield of carboxylic acid groups available for functionalization was too low to be detected with fluorescence microscopy. Another explanation that cannot be ruled out at the moment is that depolymerization was the only reaction occurring. However the use of longer SThL times did not improve the observed results. Interestingly, 15 μm × 15 μm squares activated via SThL (T_{tip} at 250 °C with v_{tip} 15 μm s^{-1}) on EGDMA cross-linked *t*BA polymer films (20 wt % EGDMA) were successfully modified with fluoresceinamine.[48]

These results demonstrate that understanding the thermal deprotection mechanism at the time scales typically used for SThL (possibly down to a few microseconds per contact point) is important for the development of nanometer sized functional surface domains with SThL. In addition, the enhanced understanding might result in the development of improved platforms for SThL. For instance, to use methacrylate based films without

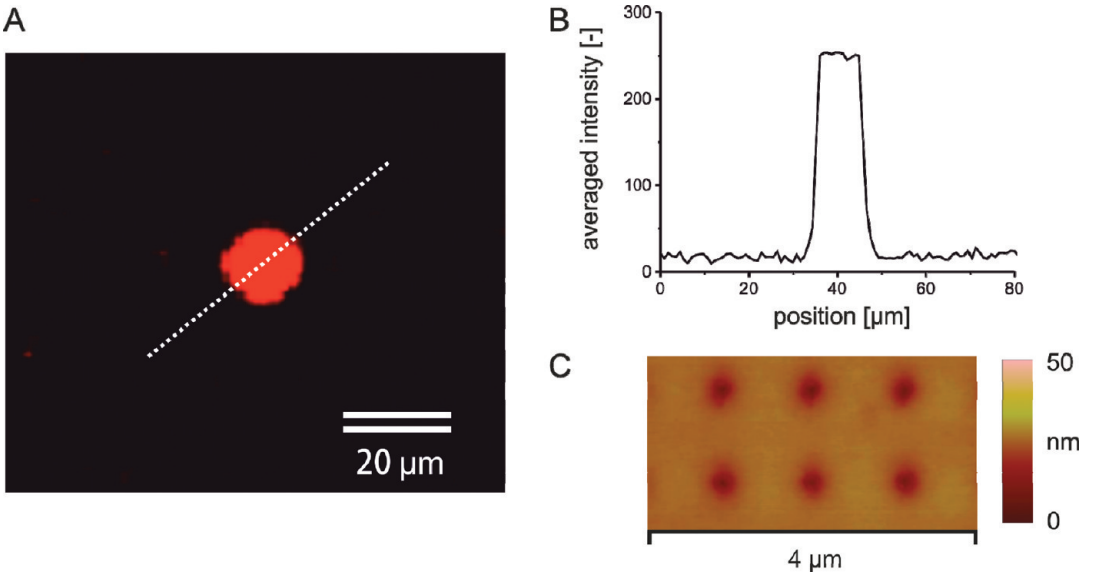

Figure 6. (A) Confocal fluorescence microscopy image (λ_{ex} = 488 nm) of a 10 μm × 10 μm square (x-y separation 1100 nm) prepared on an A_{15} film by SThL through indenting a 10 × 10 point array (x-y separation 1100 nm) with a heated probe (T_{tip} =280 °C), subsequently chemically grafted with amino functionalized eFluor 605 quantum dots ($\lambda_{em} \approx$ 605 nm) utilizing EDC/NHS activation. The probe contact load was ~20 nN, whereas the contact time of the heated probe for every point was 1 s. (B) Intensity profile along the white dashed line in A. (C) Contact mode AFM height image of a part of the freshly prepared dot array.

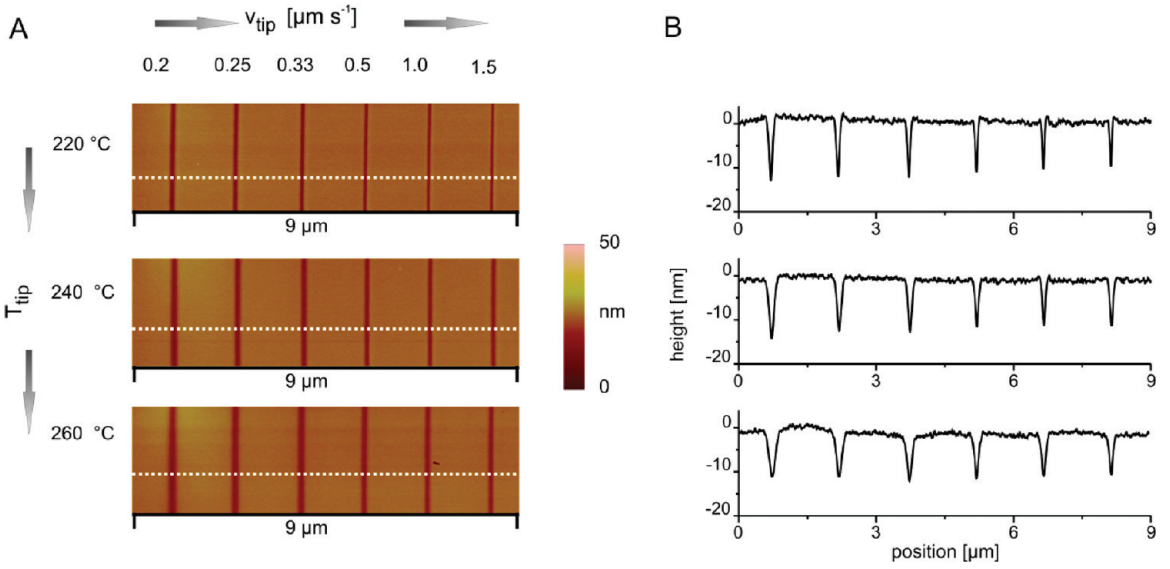

Figure 7. (A) Tapping mode AFM height images of MA_{20} after SThL of 4 μm long lines written with T_{tip} at 220 °C, 240 and 260 °C at writing speeds ranging between 0.2 and 1.5 μm s^{-1}. In B the corresponding cross sections along the white dashed lines are shown.

the undesired depolymerization reaction that is dominant at the very low thermal decomposition time scales used in SThL, one might consider the use of an ester substituent that decomposes at temperatures below which depolymerization reactions occur. King and co-workers[37,38] successfully incorporated ester substituents based on tetrahydropyranyl in cross-linked methacrylate films for SThL. In subsequent wet chemical grafting reactions, they demonstrated the wide variety in chemical functionalities that could possibly be incorporated in these films. However, the interpretation that the >100 nm deep surface depressions in P*t*BMA homopolymer films after SThL are solely ascribed to thermomechanical surface deformation may require adjustments. As shown above (Figure 5A), the depressions are also consistent with pronounced depolymerization. However, because the deprotection temperature was much higher than the glass transition temperature of P*t*BMA, it is most likely a combination of both processes.

3.5. SThL on MA_{20} Samples. Figure 7 shows TM-AFM images acquired with super sharp silicon tips (nominal tip radius $r_{tip} \approx$ 2 nm) and corresponding horizontal cross sections of grooves prepared with SThL on MA_{20} films as a function of the tip velocity (left to right) and T_{tip} (top to bottom). r_{tip} of the heated probe, determined via scanning an array of sharp tips,[49] was calculated to be approximately 40 nm. Figure 8 shows the

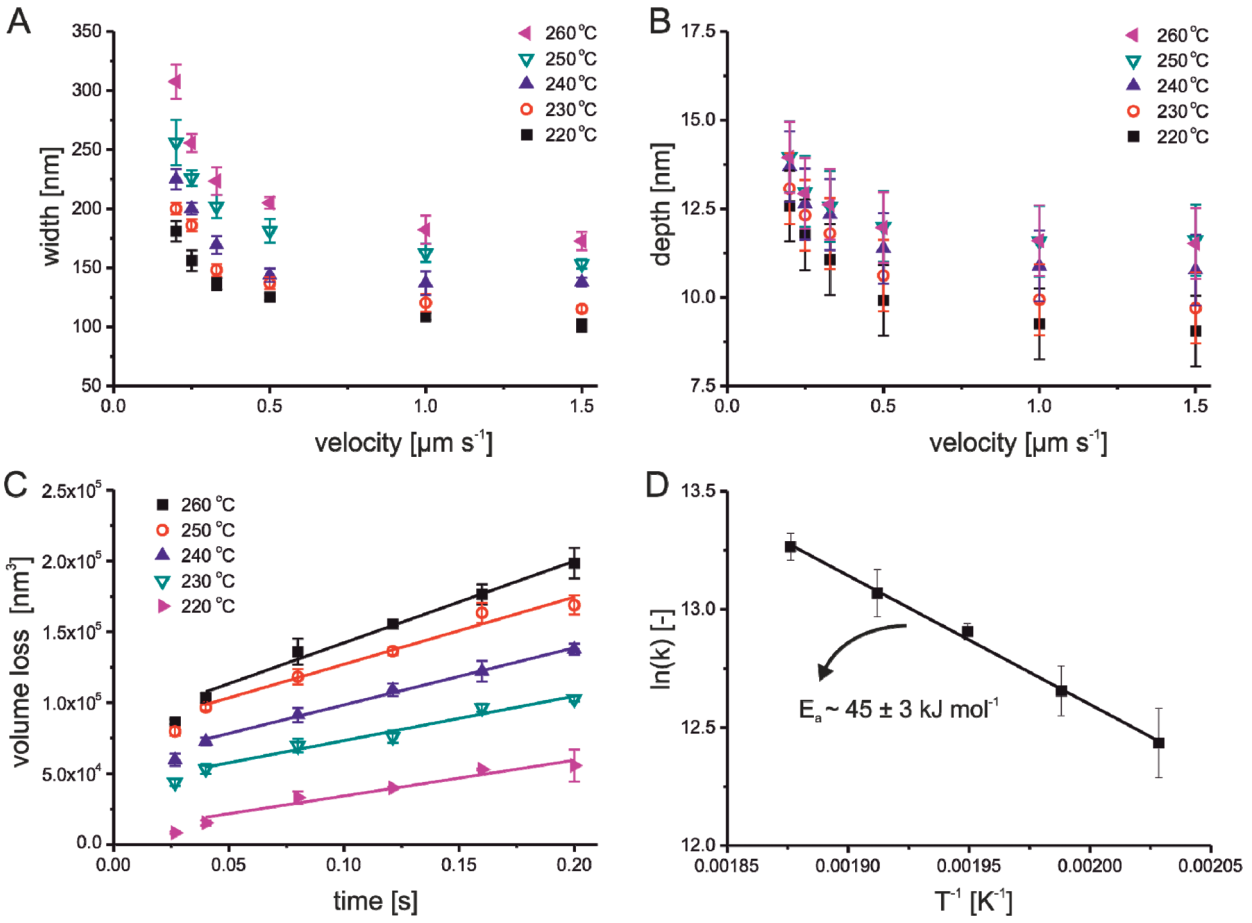

Figure 8. (A) Width and (B) depth of lines prepared by SThL in MA_{20} as a function of v_{tip} for various T_{tip}. Lines of 4 μm in length were written with a contact load of ~10 nN. (C) Volume loss as a function of the tip contact time. The solid lines correspond to linear least-squares fits of the data, corresponding to zero order reaction kinetics. (D) Arrhenius plot of the zero order reaction rate constants obtained from the linear fits in C. The solid line represents a linear least-squares fit to the data.

groove width (A) and depth (B) as a function of T_{tip} and tip velocity (v_{tip}) observed on MA_{20} samples. T_{tip} was in the range of 220 °C up to 260 °C and v_{tip} was between 0.2 and 1.5 μm s^{-1}.

From Figures 7 and 8A,B, it is clear that with decreasing T_{tip} and increasing v_{tip}, the groove width and depth decreased from ~307 to ~101 nm and ~13.7 to ~9.8 nm, respectively. This is in agreement with the expected conversion of MA_{20} upon decomposition, which is lower for shorter reaction times and lower temperatures (compare Figure 4).

The analysis of the volume loss as a function of the averaged thermolysis time for the different T_{tip} used is presented in Figure 8C. The averaged contact time was defined as the tip radius (~40 nm) devided by the tip velocity (nm s^{-1}). Allthough the contact area between the heated probe tip and the sample is much smaller that the tip radius, recent published results (see ref 28) have shown that the area near the contact point is heated efficiently, whereas a sharp decay in surface temperature exists in the radial direction. For averaged times ranging between 40 and 200 ms, the volume loss was found to be linear in time. For a thermolysis time of ~26 ms, deviations from this linear behavior was observed; therefore, these data points were not taken into account for the following calculation. It was assumed that the observed volume loss is directly proportional to the conversion of the thermal decomposition reaction, yielding presumably mainly *t*BMA monomer and small amounts of isobutylene. In Figure 8D, the corresponding Arrhenius plot is shown. An E_a for groove formation of 45 ± 3 kJ mol^{-1} was calculated.

This significantly lower value of E_a compared to the *tert*-butyl ester reaction further strengthens the assumption that depolymerization is the primary reaction for MA_{20} for the short reaction times used. The E_a for MA_{20} decomposition between 98 and 95 wt % residual mass of the TGA data presented in Figure 2A was calculated to be 112 ± 11 kJ mol^{-1}, representing a part of the reaction in which depolymerization is assumed to be the primary mechanism. However, the SThL was performed in air, whereas TGA was performed under nitrogen. For comparison, the oxidative degradation of poly(methyl methacrylate) (PMMA), yielding monomer in quantitative amounts, was reported to possess an activation energy of ~64 kJ mol^{-1}, whereas the E_a for the reaction in nitrogen was reported to be ~233 kJ mol^{-1}, respectively.[50]

The calibrated T_{tip} used for the calculation of the E_a for groove formation in MA_{20} films (45 ± 3 kJ mol^{-1}) is assumed to be the isothermal reaction temperature in close proximity of the tip−sample contact point. However, a sharp temperature gradient can be expected within radial distances of approximately 1 μm from the tip−surface contact point.[51] Lowering the set T_{tip} by, for example, 40 °C to get a more realistic effective reaction temperature will decrease the calculated E_a for groove formation by no more than 6.5 kJ mol^{-1}.

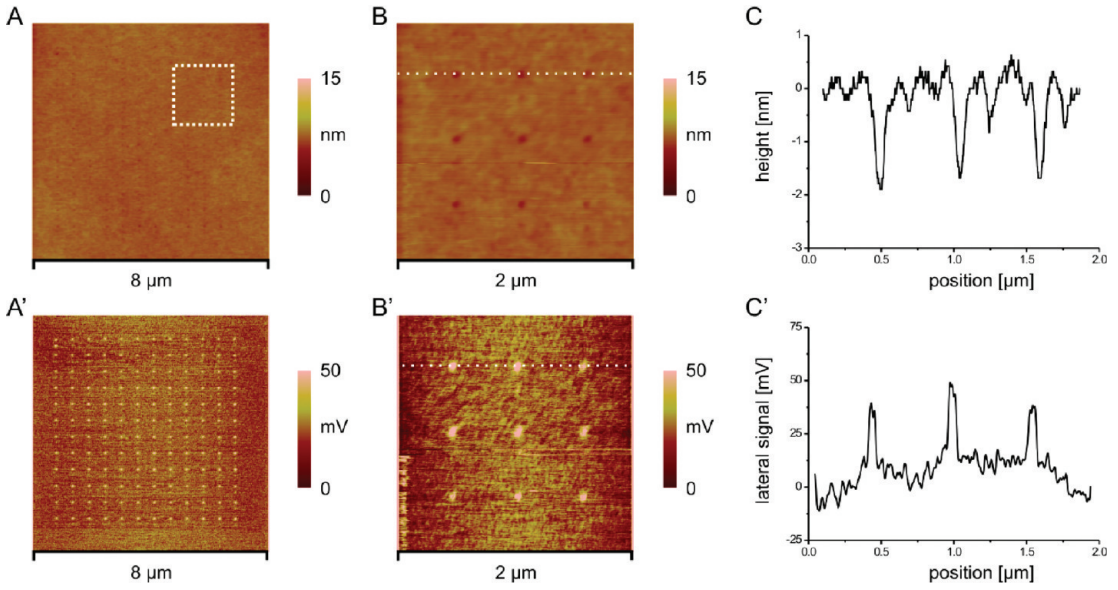

Figure 9. Contact mode AFM height images (A and B) of an 12 by 12 array prepared on an A_{20} film via SThL film with T_{tip} at 280 °C and probe contact times of 2 s while maintaining a contact force of ~5 nN. LFM images of the respective areas are shown in (A′ and B′). In C and C′ the cross-sections along the white dashed lines are shown, respectively.

3.6. SThL on A_{20} Films. Based on the relatively higher E_a values determined for the *tert*-butyl ester decomposition compared to depolymerization, we expected to significantly decrease the pattern sizes prepared with SThL on A_{20} films in which no depolymerization reactions occur. Figure 9 shows AFM images of a 12 × 12 array of dots (x-y separation 550 nm) prepared by contacting an A_{20} film with a heated tip ($T_{tip} \approx 280$ °C, probe contact time 2 s). Features with an increased lateral force signal were observed, which is in accordance with the formation of surface exposed carboxylic acid groups in these domains. The domain diameter was estimated from the LFM images to be 60 ± 8 nm, which is about 1.5 times of the approximate tip radius of the used probe (~ 40 nm). Despite the much higher contact time compared to the averaged contact times used for the grooves formed in MA_{20} films (compare Figures 10 and 11) the domain size of the individual depressions in A_{20} films is significantly reduced.

To compare SThL on MA_{20} and A_{20} films, we wrote lines with identical settings on both films. T_{tip} was set to 280 °C, and a tip velocity of 1 μm s^{-1} was used. Furthermore, the role of the size of the tip radius on the pattern size was elucidated. The results are shown in Table 1, which also includes the ultimate resolution obtained for SThL on MA_{20} and A_{20} films with empirically determined optimal settings.

From Table 1, it is clear that for the identical settings the line width in MA_{20} is approximately 10.3 and 9.8 times higher compared to those on A_{20} for r_{tip} of ~40 and ~100 nm, respectively. Furthermore, the increase in r_{tip} by a factor of 2.5 resulted in an increase in observed line widths of approximately 1.9 and 2.0 times for MA_{20} and A_{20} films, respectively. Applying a simple Hertz model[52] for the contact area between the heated probe and the flat polymer surface the increase in surface contact area was calculated as ~1.8 times. From the simple Hertz contact model, one can calculate that $(r_1/r_2)^{2/3} \approx (a_1/a_2)$, in which r represents the tip radius and a represents the contact area. Hence, it was calculated for increasing the tip radius from 40 to 100 nm (all other parameters remain the same) that the contact area would increase with a factor of ~1.8. This is in good agreement with the increase in line widths obtained after SThL for both the MA_{20} as well as the A_{20} films for the two tip radii. Ultimately, the thinnest grooves written with SThL ($r_{tip} \approx 40$ nm) in MA_{20} films were 83 ± 7 nm in width. The sufficiently high rate of the depolymerization reaction of the MA_{20} film allowed the fast writing of patterns at speeds up to 500 μm s^{-1} and higher. By contrast, lines written this fast on A_{20} films did not show any change in topography and lateral force. Lines written with SThL at 5 μm s^{-1} provided line widths of approximately 21 nm as was observed with LFM. This was about half the size of the estimated tip radius used.

Table 1. Measured Line Width and Depth Values for MA_{20} and A_{20} Films after SThL with Probes Possessing a Different Tip Radius, and Optimized Settings for Achieving the Highest Spatial Resolution with SThL on MA_{20} and A_{20} Films

film	r_{tip} (nm)	T_{tip} (°C)	F (nN)	v_{tip} (μm s^{-1})	width (nm)[a]	depth (nm)[a]
MA_{20}	40	280	~ 20	1	412 ± 37	11 ± 1
MA_{20}	100	280	~ 20	1	781 ± 70	13 ± 1
A_{20}	40	280	~ 20	1	40 ± 4[b]	n.d.
A_{20}	100	280	~ 20	1	80 ± 7[b]	n.d.
MA_{20}	40	240	~ 30	500	83 ± 7[c]	<1
A_{20}	40	280	~ 75	5	21 ± 2[b]	n.d.

[a] No tip deconvolution was applied. [b] Measured from LFM images. [c] Signs of thermomechanical deformations were observed.

The optimized settings resulted in r_{tip} to line width ratios of ~0.5 and ~2.0 for SThL on MA_{20} and A_{20}, respectively. Cacialli and co-workers[53] have reported on thermal chemical ~30 nm patterning of poly(*p*-phenylene vinylene) with a tip with an estimated 100 nm contact radius. The achieved r_{tip} to line width ratio equals in this case approximately 3.6. This increase in pattern formation aspect ratio is related to the fact that the thermal probes as used throughout our experiments have a

12 μm × 12 μm heater area positioned at the cantilever end above the tip. Therefore the heat source, although highly localized, is much more complex than the heated tip alone. Significant surface heating during SThL of polymers for example must be taken into account in order to achieve the highest possible resolution for SThL.[51]

To be able to achieve higher writing speeds for SThL films based on protected acrylates, we propose tuning the ester group to lower E_a for faster thermolysis of the ester bond. In contrast, as we have shown for the fast depolymerization reaction, much higher writing speeds were obtained, with a penalty in achievable resolution for comparable tip temperatures. Hence an optimum is expected for the choice of ester group and writing speed, with respect to patterning resolution. Operating many probes parallel, in specially designed cantilever arrays (e.g., IBM Millipede),[54] enhances the pattering throughput with an order of 1000 or more. Future efforts should be made in these directions, in order to convert SThL as an attractive technique for lab scale prototyping of, for example, biosensors into an established, widely applicable, and commercially viable approach for large-scale area patterning with sub-20 nm spatial resolution.

4. CONCLUSIONS

SThL on MA_{20} and A_{20} cross-linked films was explored in detail for the spatially controlled, highly localized thermal chemical surface functionalization of polymer interfaces. These (meth-)acrylate tailored interfaces were shown to possess an improved thermomechanical stability during SThL, enabling the writing of patterns without plastic deformation. On the basis of the observed differences in thermal chemical decomposition mechanisms for the methacrylate and acrylate based films, i.e., mainly depolymerization versus ester decomposition, respectively, the observed dissimilarities in pattern formation were explained. As a result of these differences, lines prepared in A_{20} films were typically ~10 times smaller in width compared to lines written in MA_{20} films. The smallest line width obtained was 21 ± 2 nm for SThL on A_{20} films. In order to further enhance SThL for a broader utilization, the ester groups embedded in our platforms should be tailored toward higher rate constants and a large E_a for thermolysis, enabling a faster local thermal chemical conversion of the interface.

■ ASSOCIATED CONTENT

Ⓢ Supporting Information. Additional results for the MA_{20} and A_{20} film formation as well as for the FTIR spectroscopy of the gaseous reaction products during thermal degradation of MA_{20} and A_{20} bulk samples is provided. This information is available free of charge via the Internet at http://pubs.acs.org/.

■ AUTHOR INFORMATION

Corresponding Author

*E-mail: schoenherr@chemie.uni-siegen.de (H.S.); g.j.vancso@tnw.utwente.nl (G.J.V.).

Present Addresses

[†]Department of Physical Chemistry I, University of Siegen, Faculty of Science and Technology, Adolf-Reichwein-Strasse 2, 57076 Siegen, Germany.

■ ACKNOWLEDGMENT

This work was supported by NanoImpuls/NanoNed, the nanotechnology program of the Dutch Ministry of Economic Affairs (Grant TPC.6940) and by the NWO Middelgroot Grant 700.54.102.

■ REFERENCES

(1) Salaita, K.; Wang, Y.; Mirkin, C. A. *Nat. Nanotechnol.* **2007**, *2*, 145–155.
(2) Wouters, D.; Schubert, U. S. *Angew. Chem,. Int. Ed.* **2004**, *43*, 2480–2495.
(3) Krämer, S.; Fuierer, R. R.; Gorman, C. B. *Chem. Rev.* **2003**, *103*, 4367–4418.
(4) García, R.; Martinez, R. V.; Martinez, J. *Chem. Soc. Rev.* **2006**, *35*, 29–38.
(5) Arnold, M.; Schwieder, M.; Blümmel, J.; Cavalcanti-Adam, E. A.; López-Garcia, M.; Kessler, H.; Geiger, B.; Spatz, J. P. *Soft Matter* **2009**, *5*, 72–77.
(6) Alves, N. M.; Pashkuleva, I.; Reis, R. L.; Mano, J. F. *Small* **2010**, *6*, 2208–2220.
(7) Martinez, E.; Engel, E.; Planell, J. A.; Samitier, J. *Ann. Anat.* **2009**, *191*, 126–135.
(8) Lussi, J. W.; Michel, R.; Reviakine, I.; Falconnet, D.; Goessl, A.; Csucs, G.; Hubbell, J. A.; Textor, M. *Prog. Surf. Sci.* **2004**, *76*, 55–69.
(9) Jonkheijm, P.; Weinrich, D.; Schröder, H.; Niemeyer, C. M.; Waldmann, H. *Angew. Chem,. Int. Ed.* **2008**, *47*, 9618–9647.
(10) LaFratta, C. N.; Walt, D. R. *Chem. Rev.* **2008**, *108*, 614–637.
(11) Lei, Y.; Yang, S.; Wu, M.; Wilde, G. *Chem. Soc. Rev.* **2011**, *40*, 1247–1258.
(12) Sepúlveda, B.; Angelomé, P. C.; Lechuga, L. M.; Liz-Marzán, L. M. *Nano Today* **2009**, *4*, 244–251.
(13) Mamin, H. J. *Appl. Phys. Lett.* **1996**, *69*, 433–435.
(14) Vettiger, P.; Despont, M.; Drechsler, U.; Dürig, U.; Häberle, W.; Lutwyche, M. I.; Rothuizen, H. E.; Stutz, R.; Widmer, R.; Binnig, G. K. *IBM J. Res. Dev.* **2000**, *44*, 323–340.
(15) Christman, K. L.; Schopf, E.; Broyer, R. M.; Li, R. C.; Chen, Y.; Maynard, H. D. *J. Am. Chem. Soc.* **2009**, *131*, 521–527.
(16) Tseng, A. A. *Small* **2005**, *1*, 924–939.
(17) Binnig, G. K.; Cherubini, G.; Despont, M.; Dürig, U. T.; Eleftheriou, E.; Pozidis, H.; Vettiger, P. In: Bhushan, B., Ed. *Handbook of Nanotechnology*, 2nd ed.; Springer Science and Business Media Inc.: Heidelberg, Germany, 2006; pp 1457−1486.
(18) Salaita, K.; Wang, Y. H.; Fragala, J.; Vega, R. A.; Liu, C.; Mirkin, C. A. *Angew. Chem., Int. Ed.* **2006**, *45*, 7220–7223.
(19) Lenhert, S.; Sun, P.; Wang, Y. H.; Fuchs, H.; Mirkin, C. A. *Small* **2007**, *3*, 71–75.
(20) Kaufmann, T.; Ravoo, B. J. *Polym. Chem.* **2010**, *1*, 371–387.
(21) Xia, Y.; Whitesides, G. M. *Angew. Chem., Int. Ed.* **1998**, *37*, 550–575.
(22) Weibel, D. B.; DiLuzio, W. R.; Whitesides, G. M. *Nat. Rev. Microbiol.* **2007**, *5*, 209–218.
(23) Truskett, V. N.; Watss, M. P. C. *Trends Biotechnol.* **2006**, *24*, 312–317.
(24) Guo, L. J. *J. Phys. D: Appl. Phys.* **2004**, *37*, R123–R141.
(25) Chou, S. Y.; Krauss, P. R.; Renstrom, P. J. *Science* **1996**, *272*, 85–87.
(26) Chou, S. Y.; Krauss, P. R.; Renstrom, P. J. *Appl. Phys. Lett.* **1995**, *67*, 3114–3116.
(27) La, Y. H.; Stoykovich, M. P.; Park, S. M.; Nealey, P. F. *Chem. Mater.* **2007**, *19*, 4538–4544.
(28) La, Y. H.; Edwards, E. W.; Park, S. M.; Nealey, P. F. *Nano Lett.* **2005**, *5*, 1379–1384.
(29) Böker, A.; Reihs, K.; Wang, J. G.; Stadler, R.; Ober, C. K. *Macromolecules* **2000**, *33*, 1310–1320.
(30) Böker, A.; Herweg, T.; Reihs, K. *Macromolecules* **2002**, *35*, 4929–4937.

(31) Duvigneau, J.; Cornelissen, S.; Bardají Valls, N.; Schönherr, H.; Vancso, G. J. *Adv. Funct. Mater.* **2010**, *20*, 460–468.
(32) Duvigneau, J.; Schönherr, H.; Vancso, G. J. *Langmuir* **2008**, *24*, 10825–10832.
(33) Feng, C. L.; Vancso, G. J.; Schönherr, H. *Langmuir* **2007**, *23*, 1131–1140.
(34) Feng, C. L.; Vancso, G. J.; Schönherr, H. *Langmuir* **2005**, *21*, 2356–2363.
(35) Feng, C. L.; Embrechts, A.; Vancso, G. J.; Schönherr, H. *Eur. Polym. J.* **2006**, *42*, 1954–1965.
(36) Feng, C. L.; Embrechts, A.; Bredebusch, I.; Bouma, A.; Schnekenburger, J.; García-Parajó, M.; Domschke, W.; Vancso, G. J.; Schönherr, H. *Eur. Polym. J.* **2007**, *43*, 2177–2190.
(37) Szoszkiewicz, R.; Okada, T.; Jones, S. C.; Li, T. D.; King, W. P.; Marder, S. R.; Riedo, E. *Nano Lett.* **2007**, *7*, 1064–1069.
(38) Wang, D. B.; Kodali, V. K.; Underwood, W. D.; Jarvholm, J. E.; Okada, T.; Jones, S. C.; Rumi, M.; Dai, Z. T.; King, W. P.; Marder, S. R.; Curtis, J. E.; Riedo, E. *Adv. Funct. Mater.* **2009**, *19*, 3696–3702.
(39) Grassie, N. *Pure Appl. Chem.* **1972**, *30*, 119–134.
(40) Grant, D. H.; Grassie, N. *Polymer* **1960**, *1*, 125–134.
(41) Alfrey, T.; Haas, H. C.; Lewis, C. W. *J. Am. Chem. Soc.* **1951**, *73*, 2851–2853.
(42) Odian, G. *Principles of Polymerization*, 3rd ed.; John Wiley & Sons Inc.: New York, 1991; p 692.
(43) Schaefgen, J. R.; Sarasohn, I. M. *J. Polym. Sci.* **1962**, *58*, 1049–1061.
(44) Litmanovich, A. D.; Cherkezyan, V. O. *Eur. Polym. J.* **1984**, *20*, 1041–1044.
(45) Carpick, R. W.; Salmeron, M. *Chem. Rev.* **1997**, *97*, 1163–1094.
(46) Morgenthaler, S. M.; Lee, S.; Spencer, N. D. *Langmuir* **2006**, *22*, 2706–2711.
(47) Sasaki, K.; Koike, Y.; Azehara, H.; Hokari, H.; Fujihira, M. *Appl. Phys. A: Mater. Sci. Process* **1998**, *66*, S1275–S1277.
(48) Duvigneau, J.; Schönherr, H.; Vancso, G. J. *MRS Proc.* **2011**, *1318*, vv-04–07.
(49) Bykov, V.; Gologanov, A.; Shevyakov, V. *Appl. Phys. A: Mater. Sci. Process* **1998**, *66*, 499–502.
(50) Kashiwagi, T.; Hirata, T.; Brown, J. E. *Macromolecules* **1985**, *18*, 131–138.
(51) Duvigneau, J.; Schönherr, H.; Vancso, G. J. *ACS Nano* **2010**, *4*, 6932–6940.
(52) Hertz, H. J. *Reine Angew. Math.* **1881**, *92*, 156–171.
(53) Fenwick, O.; Bozec, L.; Credgington, D.; Hammiche, A.; Lazzerini, G. M.; Silberberg, Y. R.; Cacialli, F. *Nat. Nanotechnol.* **2009**, *4*, 664–668.
(54) Binnig, G. K.; Cherubini, G.; Despont, M.; Dürig, U. T.; Eleftheriou, E.; Pozidis, H.; Vettiger, P. In: Bhushan, B., Ed. *Handbook of Nanotechnology*, 2nd ed.; Springer Science and Business Media Inc.: Heidelberg, Germany, 2006; pp 1457−1486.
(55) Abel, M. R.; Wright, T. L.; King, W. P.; Graham, S. *IEEE Trans. Compon. Packag. Technol.* **2007**, *30*, 200.